J Solid State Electrochem (2010) 14:1637–1647
DOI 10.1007/s10008-010-1002-3

ORIGINAL PAPER

Electrocatalytic oxidation and sensitive detection of deferoxamine on nanoparticles of Fe_2O_3@NaCo[Fe(CN)$_6$]-modified paste electrode

H. Heli · S. Majdi · N. Sattarahmady · A. Parsaei

Received: 11 August 2009 / Revised: 12 December 2009 / Accepted: 3 January 2010 / Published online: 2 February 2010

Abstract Electrocatalytic oxidation of deferoxamine was studied on carbon paste electrodes modified with nanoparticles of iron(III) oxide core-cobalt hexacyanoferrate-shell using cyclic voltammetry and chronoamperometry. Voltammetric curves represented two quasi-reversible redox transitions which in the presence of deferoxamine, the two anodic peak currents increased, followed by decreases in the corresponding cathodic currents. This indicated that deferoxamine was oxidized on the immobilized cobalt hexacyanoferrate via two electrocatalytic steps. The rate constants, the electron transfer coefficients and the diffusion coefficient involved in the electrocatalytic oxidation of deferoxamine were reported. A sensitive and time-saving determination procedure was developed for the analysis of the drug in both batch and flow systems, and the corresponding analytical parameters were reported. The proposed amperometric method was also successfully applied to the direct assays of spiked human serum with iron–drug complex.

H. Heli (✉)
Department of Chemistry, Islamic Azad University,
Fars Science and Research Branch,
P. O. Box: 73715-181, Marvdasht, Iran
e-mail: hheli7@yahoo.com

S. Majdi
Department of Chemistry, K. N. Toosi University of Technology,
Tehran, Iran

N. Sattarahmady
Department of Biochemistry,
Shiraz University of Medical Sciences,
Shiraz, Iran

A. Parsaei
Sobhan Oncology Co.,
Tehran, Iran

Keywords Deferoxamine · Desferal · Nanoparticles · Core-shell structure · Electrocatalysis · Cobalt hexacyanoferrate

Introduction

In the thalassemias, the synthesis of an alpha or beta globin chain of hemoglobin is ceased or decreased. This creates a deficiency of hemoglobin in each red blood cell. More importantly, the excess unmatched globin chains accumulate in the growing erythroid precursors, causing hemolysis and ineffective erythropoiesis. Patients with these syndromes require regular blood transfusions to maintain a hemoglobin level of around 1.2 g mL^{-1}, which subsequently leads to iron overload. High level of iron is toxic and can be fatal if untreated.

Diseases associated with iron overload are usually treated with iron chelators like deferoxamine (DFO). DFO scavenges iron from cells so prevents both host cells and microorganisms from accessing to iron. DFO can also be used to bind to and remove aluminum [1]. As DFO is removed from the body after binding to excess iron and aluminum, it reduces iron or aluminum deposits in the organs or tissues.

Nanostructured materials are of great interest in the advanced materials world due to their chemical, physical, and biological (e.g. special electronic, catalytic, optical, and magnetic) properties when compared to the corresponding atoms/molecules or their bulk states. These unique properties are results of effects that take over on the nanosize dimension and high surface-to-volume ratio compared to bulk metals [2–4].

Nanostructured materials often represent excellent electronic conductivity and electrocatalytic properties. These

properties accelerate the rate of direct or mediated heterogeneous electron transfer between the electrode surface and species in the solution [4–8].

Nanoparticles are divided into two categories according to their shape and geometry: isotropic and anisotropic nanoparticles. Examples for isotropic nanoparticles are nanoparticles with spherical or cubic shape. For the anisotropic nanoparticles, core-shell materials with different structures, sizes, and compositions have been recently synthesized and studied [9]. The importance of core-shell materials is due to capabilities of core and shell processibility, stability, tunability, and reactivity.

Electrochemical routes are suitable procedures for the sensitive determination of drugs and related compounds in pharmaceutical dosage forms and biological fluids [2, 4–8, 10, 11]. They have the advantages of simplicity, low cost, not requiring—in most instances—derivatization, less sensitive to matrix effects and relatively fast analysis compared with other techniques. The electrochemical methods have usually superior specificity and selectivity because the peak potentials can readily identify drugs. In addition, study of the redox properties of drugs provides insight into their metabolic fate, their in vivo redox processes, and their pharmacological activity [12].

Metal hexacyanoferrates (MHCFs) which belong to the class of polynuclear transition metal cyanides exhibit well-defined and reproducible electrochemical responses. The deliberate control of the reactivity of certain immobilized MHCFs at the electrode surface can enhance electrode reactivity and efficiency. The electrochemical studies using modified electrodes with MHCFs make them suitable for various applications in ion selective sensors [13], display [14], solid-state batteries [15] and electrocatalysis and electroanalysis [16].

Among the MHCFs, cobalt hexacyanoferrate (CoHCF) has been widely used for preparing modified electrodes using different methods of synthesis. CoHCF is formed as a thin film on electrode surfaces; for example, a thin film of CoHCF was formed using electroless technique [17]. Moreover, stable electroreactive thin films of CoHCF were electrochemically deposited on the surface of a microband gold [18], glassy carbon [19] and Pt and Au [20] electrodes. A CoHCF film was also formed on multiwall carbon nanotube modified gold electrode from the solution using electrodeposition method and CoHCF nanowires were finally obtained [21].

Continuing our recent works on the electrocatalysis and electroanalysis of drugs and biologically active compounds [2–8, 10, 11], in the present work, the electrocatalytic oxidation and determination of DFO at nanoparticles of Fe_2O_3 core-$NaCo[Fe(CN)_6]$-shell (n-Fe_2O_3@$NaCo[Fe(CN)_6]$)-modified carbon paste electrode (n-CPE) has been investigated.

Experimental section

Materials

All chemicals were of analytical grade from Merck or Sigma and were used without further purification. DFO was received from Novartis Pharma AG, Basel, Switzerland. All solutions were prepared with doubly distilled water.

Synthesis of nanoparticles of Fe_2O_3 (n-Fe_2O_3)

Five milliliters of aerated iron ion solution of 0.10 M Fe^{2+}+ 0.20 M Fe^{3+} was added dropwise into 50 mL of aerated 2 M sodium hydroxide solution under vigorous mechanical stirring for 30 min at 80°C. The precipitated product was collected and washed with redistilled water. After washing, 10 mL of 10 mM HCl solution was added. n-Fe_2O_3 was collected and removed from the solution by filtration. The chemical reactions of Fe_2O_3 formation are:

$$Fe^{2+} + Fe^{3+} + O_2 + 2\,OH^- \rightarrow Fe_2O_3 + H_2O \quad (1)$$

$$2\,Fe_3O_4 + 1/2\,O_2 \rightarrow 3\,Fe_2O_3 \quad (2)$$

Synthesis of n-Fe_2O_3@$NaCo[Fe(CN)_6]$

Fe_2O_3 nanoparticles were suspended in 10 mL of a solution of 0.10 M $Na_3[Fe(CN)_6]$ containing 10 mmol L^{-1} HCl and stirred for about 30 min. Then 10 mL of 0.10 M $CoCl_2$ solution containing 10 M HCl was added, and the resultant mixture was stirred for 30 min. Subsequently, the obtained n-Fe_2O_3@$NaCo[Fe(CN)_6]$ was collected and washed with 10 mM HCl solution until the washing solution became colorless and then washed with redistilled water. The particles were dried in a vacuum at room temperature.

Apparatus

Electrochemical measurements were carried out in a conventional three-electrode cell powered by an electrochemical system comprising of a μ-Autolab, type III potentiostat/galvanostat (The Netherlands). An Ag/AgCl, 3 M KCl and a platinum disk (both from Azar electrode Co., Iran) were used as reference and auxiliary electrodes, respectively. The system was run by a PC through the GPES 4.9 software.

Surface morphological studies were carried out using scanning electron microscopy (SEM) on a Model X-30Philips instrument. The transmission electron microscopy (TEM) was performed using a CEM 902A ZEISS transmission electron microscope, with an accelerating voltage of

80 kV. These techniques provided information about the morphology and size of particles. Samples were prepared by placing a drop of the particles, dispersed in acetone, on a carbon-covered copper grid (400 mesh) and evaporating the solvent.

X-ray diffraction (XRD) patterns were measured by a Philips X'Pert, The Netherlands, using Cu Kα radiation at 40 kV and 30 mA.

Delivering the supporting electrolyte solution as the carrier stream and injection of solutions of DFO was performed by a homemade peristaltic pump using a homemade injection valve with an interconnecting Teflon tube equipped with a 100-μL sample loop. A flow rate of 1.0 mL min^{-1} was employed. A glass cell mounted in a wall-jet configuration utilized a conventional three-electrode set-up was arranged.

Working electrodes preparation

Unmodified carbon paste electrode (u-CPE) was prepared by hand-mixing carbon powder and mineral oil (Nujol) with a 80/20% (*w*/*w*) ratio. The paste was carefully mixed and homogenized in an agate mortar for 20 min. The resulting paste was kept at room temperature in a desiccator before use. The paste was packed firmly into a cavity (3.6 mm diameter and 2 mm depth) at the end of a Teflon tube. Electrical contact was established by a copper wire connected to the paste in the inner hole of the tube. The electrode surface was gently smoothed by rubbing on a piece of weighing paper just prior to use. This procedure was also used to regenerate the surface of the carbon paste electrodes.

n-Fe_2O_3-modified carbon paste electrode (nc-CPE) was prepared by mixing weighed amounts of carbon powder, Nujol and n-Fe_2O_3 with ratios of 75:25:5%, *w*/*w* in an agate mortar until a uniform paste was obtained. The paste was packed into a 3-mm diameter cavity at the end of a Teflon tube and the electrical contact was provided with a copper wire. n-CPE was prepared in similar way otherwise that n-Fe_2O_3@NaCo[$Fe(CN)_6$] was employed as the paste modifier.

Procedures

The standard solutions of DFO were prepared by dissolving accurate mass of the bulk drug in an appropriate volume of 100 mM phosphate buffer solution, pH 7.4 (PBS, which was also used as running electrolyte throughout the work). The solutions were then stored in the dark at 4°C. Additional dilute solutions were prepared daily by accurate dilution just before use. The drug solutions were stable, and their concentrations did not change with time.

The calibration curve for the drug in PBS was measured with an amperometric technique in bath system. Working potentials of 480 or 900 mV were used in amperometric measurements, in which the transient currents were allowed to decay to steady-state values.

In the course of the development of analytical procedures for analysis of DFO in other matrix, we used the standard addition method in order to prevent the interference of other chemicals which may be present in the matrices.

DFO and DFO–iron complex-free serum samples were obtained from healthy male volunteers and stored frozen until the time of assay. The serum samples were diluted (1:7) with the supporting electrolyte and filtrated through a 30 kDa filter to produce protein-free human serum. Various portions of stock DFO solution were transferred into 10 mL volumetric flasks containing 3.3 mL of the serum sample. These solutions were then diluted to the mark with the supporting electrolyte for preparation of spiked samples (final dilution of 1:10 with the supporting electrolyte). The protein-free spiked serum solutions were directly analyzed by the calibration method, according to the proposed procedure. The calibration curves for the complex of DFO–iron in human serum blood samples were measured with the amperometric technique with working potentials of 480 or 900 mV.

In flow injection analysis, before the first measurement was performed, the system was allowed to run for 5 min to achieve good mechanical and thermal stability. Potential steps of 490 or 894 mV were applied until a stable blank baseline was observed. Then the solutions were injected into the carrier stream, the current signals were recorded, and the concentration of DFO was quantified finally by the peak height of currents. All studies/measurements were carried out at room temperature.

Results and discussion

Surface morphologies of n-Fe_2O_3 and n-Fe_2O_3@NaCo[$Fe(CN)_6$] were examined by SEM and TEM. Figure 1 shows SEM (a and c) and TEM (b and d) images of n-Fe_2O_3 (a and b) and n-Fe_2O_3@NaCo[$Fe(CN)_6$] (c and d). n-Fe_2O_3 with an average size of 40 nm and n-Fe_2O_3@NaCo[$Fe(CN)_6$] with an average size of ≈60 nm in a core-shell structure with shells of 10–30 nm thickness are witnessed.

Figure 2 shows an IR spectrum of n-Fe_2O_3@NaCo[$Fe(CN)_6$]. In the spectrum, a strong band at about 2,125 cm^{-1} appears. It is close to the typical characteristic absorption peak of MHCFs, corresponding to the stretching vibration of C≡N group in n-Fe_2O_3@NaCo[$Fe(CN)_6$] [22]. Peaks at 594 and 538 cm^{-1} are referred to stretching mode of FeC and bending mode of FeCN bonds, respectively [23]. These peaks confirmed that the unit of FeCNCo existed in the structure of n-Fe_2O_3@NaCo[$Fe(CN)_6$]. A peak at 1,609 cm^{-1} is assigned to the binding vibration of crystal water contained in the structured of n-Fe_2O_3@NaCo[$Fe(CN)_6$]

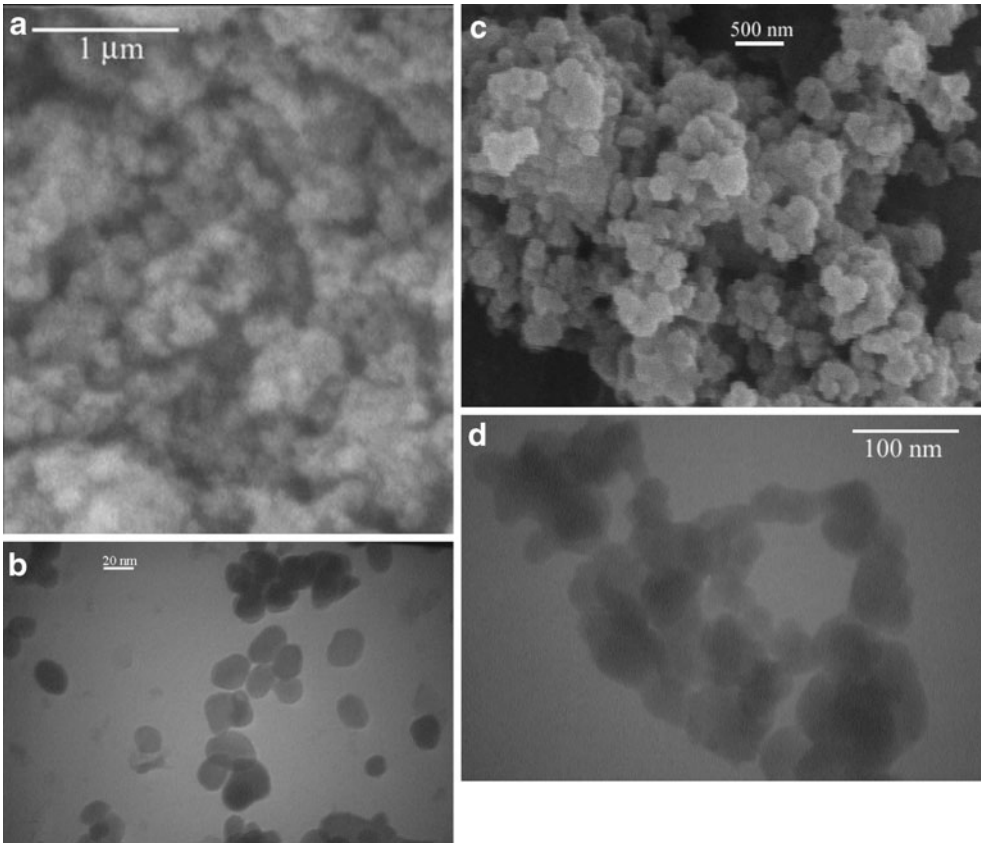

Fig. 1 SEM (**a**, **c**) and TEM (**b**, **d**) images of n-Fe_2O_3 (**a**, **b**) and n-Fe_2O_3@NaCo[$Fe(CN)_6$] (**c**, **d**)

[24]. A broadband at around 3,420 cm^{-1} showed stretching vibration of the OH group, indicating that there was H_2O in the structure of n-Fe_2O_3@NaCo[$Fe(CN)_6$]. A peak at 1,385 cm^{-1} was assigned to the stretching mode of few NO_3^- ions that adsorbed on the n-Fe_2O_3@NaCo[$Fe(CN)_6$] due to usage of $Fe(NO_3)$ in the process of synthesis [23].

Figure 3 shows X-ray diffraction patterns of as synthesized n-Fe_2O_3 (a) and n-Fe_2O_3@NaCo[$Fe(CN)_6$] (b). The patterns contained slightly broadened peaks, due to the nanometer-size effect of the samples [25]. n-Fe_2O_3 were randomly oriented polycrystalline with main diffraction peaks at (1 0 4), (1 1 0), (0 1 8), and (2 1 4). The pattern is

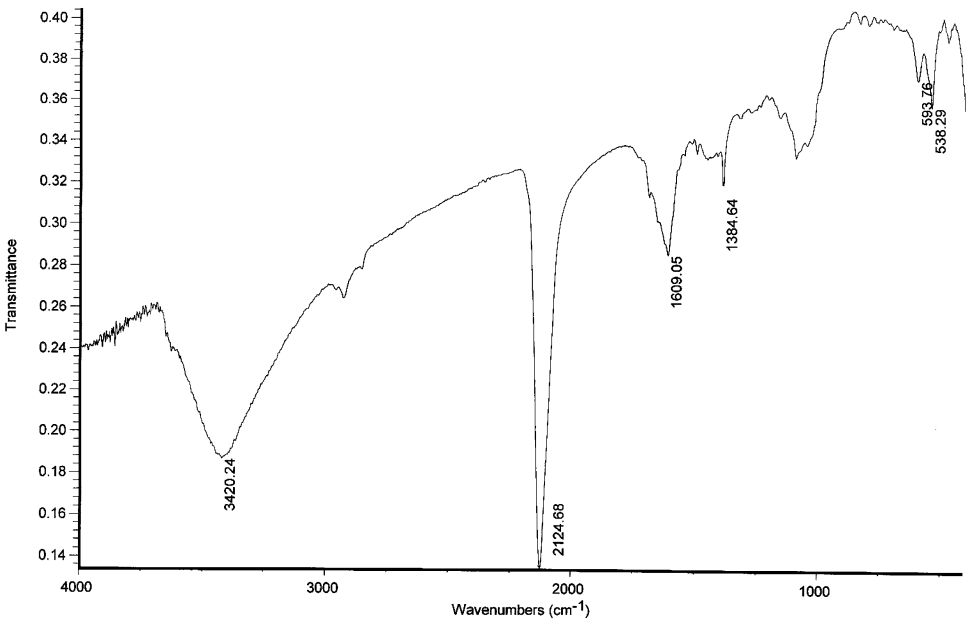

Fig. 2 IR spectra of n-Fe_2O_3@NaCo[$Fe(CN)_6$]

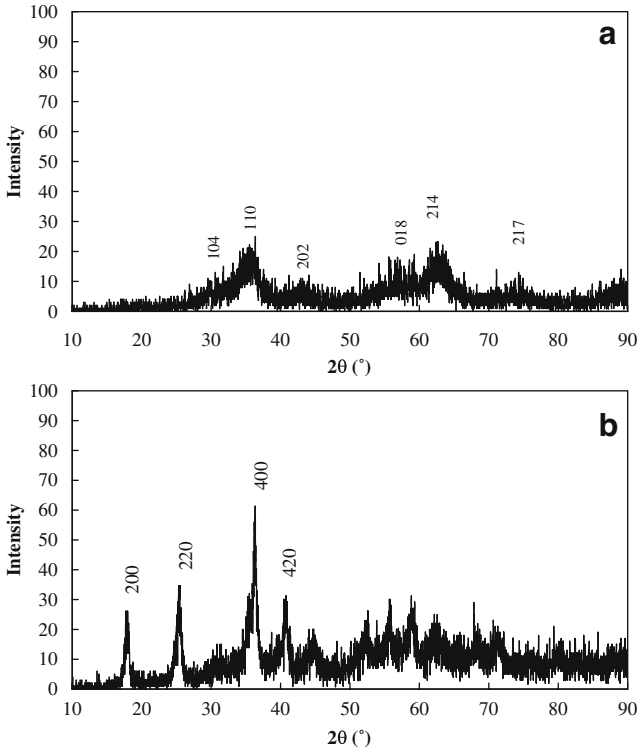

Fig. 3 X-ray diffraction patterns of n-Fe_2O_3 (**a**) and n-Fe_2O_3@NaCo[$Fe(CN)_6$] (**b**)

similar to that reported for α-Fe_2O_3 elsewhere [26]. The XRD pattern of n-Fe_2O_3@NaCo[$Fe(CN)_6$] represents major diffraction peaks corresponding to the (2 0 0), (2 2 0), (4 0 0), and (4 2 0) reflections, respectively. This pattern is also in good agreement with that reported for CoHCF prepared by chemical precipitation [27].

Figure 4 represents cyclic voltammograms of n-CPE in PBS recorded in the absence (a) and presence (b) of 0.33 mM DFO. The potential sweep rate was 50 mV s^{-1}. n-CPE exhibits two sets of quasi-reversible redox transition with the formal peak potentials (as mid-peak potentials obtained from cyclic voltammograms recorded at slow potential sweep rates of <10 mV s^{-1}) of 455 mV (denoted as transition I) and 850 mV (denoted as transition II). Transition I is assigned to the Co(III)/Co(II) redox couple, which is also supported by similar reports of cobalt in cobalt phthalocyanin and cobalt porphyrin complexes [28, 29], and transition II is related to the Fe(III)/Fe(II) redox couple which is analogous to those reported for the low spin iron in Prussian Blue [19, 30]. The electrochemical processes of redox couples I and II can be written as Eqs. 3 and 4, respectively [19, 30–33]:

for transition I:

$$NaCo^{III}\left[Fe^{II}(CN)_6\right] + Na^+ + e^- \rightleftarrows Na_2Co^{II}Fe^{II}(CN)_6 \quad (3a)$$

$$Na_{0.4}Co^{III}{}_{1.3}\left[Fe^{II}(CN)_6\right] + Na^+ + e^- \rightleftarrows Na_{1.4}Co^{II}{}_{1.3}\left[Fe^{II}(CN)_6\right] \quad (3b)$$

and for transition II:

$$Co^{II}_{1.5}\left[Fe^{III}(CN)_6\right] + Na^+ + e^- \rightleftarrows NaCo^{II}_{1.5}\left[Fe^{II}(CN)_6\right] \quad (4a)$$

$$Co^{III}\left[Fe^{III}(CN)_6\right] + Na^+ + e^- \rightleftarrows NaCo^{III}\left[Fe^{II}(CN)_6\right] \quad (4b)$$

It has been established that the structure of CoHCF is similar to those of hexacyanoferrates of copper and nickel. It easily allows the flux of alkali metal cations in the electrolyte during the redox reactions [19, 34, 35]. Transfer of electrons is always accompanied by simultaneous motion of counter cations to maintain charge balance during the redox reaction. The insertion of counter cation into the MHCF during the reduction and its exclusion upon oxidation has been verified using the electrochemical quartz crystal microbalance (EQCM) technique [19]. Along this line, cyclic voltammograms of n-CPE in PBS of various concentrations of 10–150 mM were recorded (data not shown). The anodic and cathodic currents of redox couples I and II increased following by decreasing the peak potential separation upon increasing the electrolyte concentration. In addition, the redox potentials shift in positive direction with the increase in the concentration. The reversibility of the kinetics of couples I and II was decreased upon decreasing the electrolyte concentration due to: (1) increment of the thickness of the diffusion layer of cation in the ion channel of n-Fe_2O_3@NaCo[$Fe(CN)_6$] upon decreasing the concentration of the supporting electro-

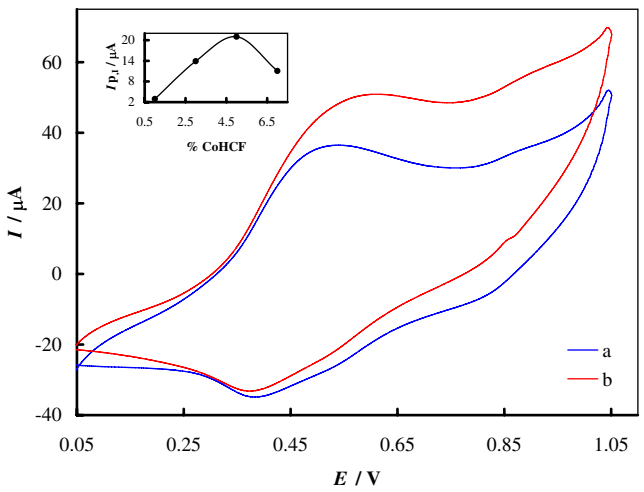

Fig. 4 Typical cyclic voltammograms of n-CPE in PBS recorded in the absence (**a**) and presence (**b**) of 0.33 mM DFO. The potential sweep rate was 50 mV s^{-1}. *inset* The effect of the quantity of n-Fe_2O_3@NaCo[$Fe(CN)_6$] added to n-CPE on the peak currents of n-CPE

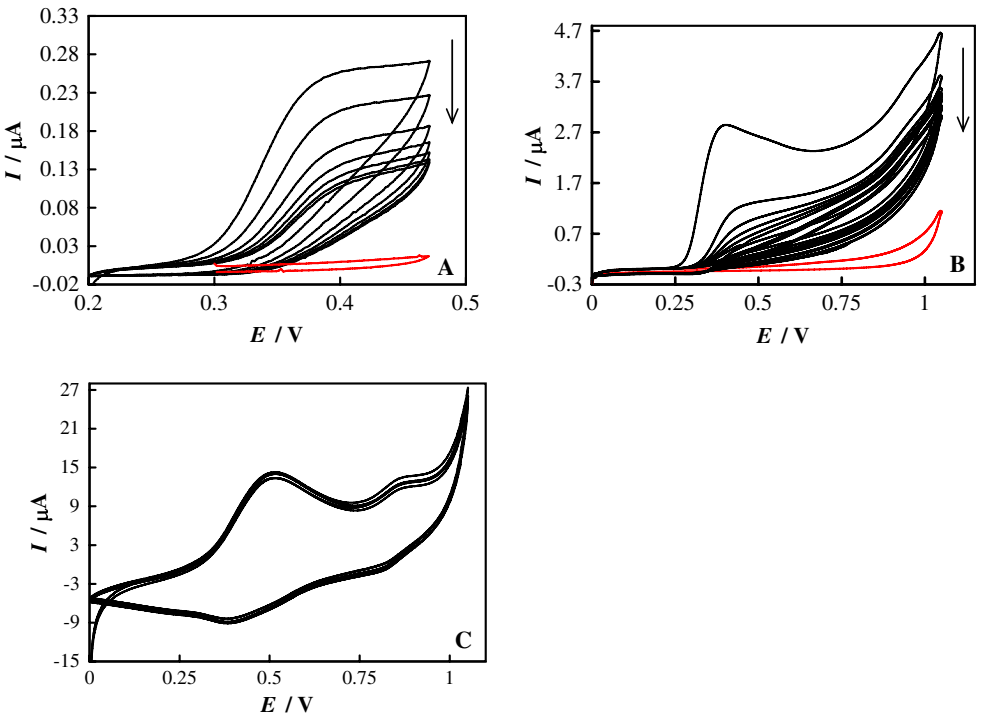

Fig. 5 **a** Consecutive voltammograms of DFO recorded using u-CPE in PBS. The potential sweep rate was 50 mV s^{-1}. **b** Consecutive voltammograms of DFO recorded using nc-CPE in PBS. The potential sweep rate was 50 mV s^{-1}. **c** Consecutive voltammograms of DFO recorded using n-CPE in PBS. The potential sweep rate was 50 mV s^{-1}. *Red lines* represent cyclic voltammograms recorded in the absence of DFO

lyte and/or (2) increasing the ohmic resistance and uncompensated resistance of the supporting electrolyte. The redox potentials of n-Fe_2O_3@NaCo[$Fe(CN)_6$] increased linearly with logarithm of the sodium ion concentration and slopes of 58.96 and 57.97 mV $decade^{-1}$ with a correlation coefficient of 0.9963 and 0.9975 for peaks I and II were obtained, respectively. These values are almost identical to the value of the Nernst slope for one-valence cation.

The effect of the quantity of n-Fe_2O_3@NaCo[$Fe(CN)_6$] added to n-CPE on the peak currents of n-CPE (in the absence of DFO) was checked. It was found that the currents of n-Fe_2O_3@NaCo[$Fe(CN)_6$] (e.g. for transition I, Fig. 4, inset) increased up to 5% *w*/*w* modifier added to the paste, and further increment caused decrease in currents. Therefore, we chose 5% *w*/*w* as optimum quantity of n-Fe_2O_3@NaCo[$Fe(CN)_6$] for the paste modification.

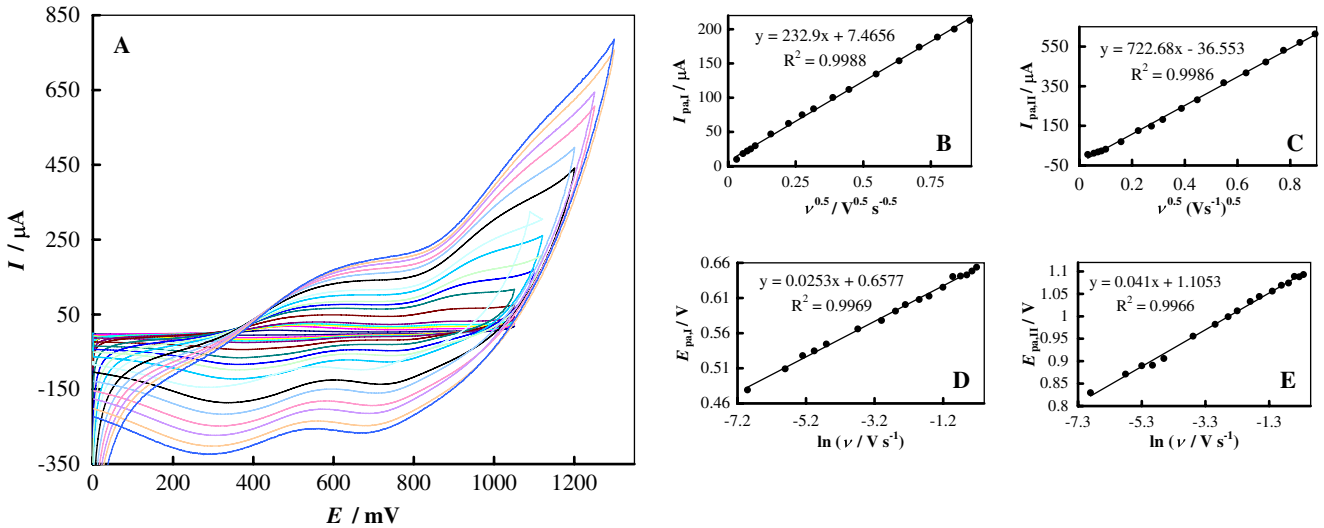

Fig. 6 **a** Cyclic voltammograms of 23.8 μM DFO in PBS using n-CPE recorded at different potential sweep rates from inner to the outer of 1, 3, 5, 7, 10, 25, 50, 75, 100, 150, 200, 300, 400, 500, 600, 700, and 800 mV s^{-1}. **b** Dependency of the anodic peak current of transition I on the square root of the potential sweep rate. **c** Dependency of the anodic peak current of transition II on the square root of the potential sweep rate. **d** Dependency of anodic peak potential of transition I on the natural logarithm of the potential sweep rate. **e** Dependency of anodic peak potential of transition II on the natural logarithm of the potential sweep rate

Upon addition of 0.33 mM DFO to the solution, enhancements of both anodic currents of transitions I and II are observed which are followed by decrements of the corresponding cathodic currents (Fig. 4, curve b). This behavior can be interpreted as electrocatalytic oxidation mechanisms. In the presence of DFO, the anodic charge associated with the anodic transition I is quantitatively ≈96% that of the corresponding cathodic peak. In the absence of DFO, this charge would be ≈70% that of the corresponding cathodic peak. For transitions II, these values are ≈73% and ≈20%, respectively. These indicate that DFO is oxidized by both active moieties of Co(III) and Fe(III) in the course of transitions I and II, respectively, via two cyclic mediation redox processes. Cobalt and iron species are present on the electrode surface, and the species with the higher valence oxidizes DFO via chemical reactions followed by generation of low-valence species. Along this line, the high-valence species are regenerated through the external electrical circuit. Accordingly, DFO is oxidized twice via two EC′ processes. Moreover, the significant currents in the reverse sweep indicate that the reactions of DFO with high-valence species are the rate-determining steps of the oxidation processes.

The overall process can be expressed as:

$$\mathrm{Co(III)} + \mathrm{e} \rightleftarrows \mathrm{Co(II)} \tag{5}$$

$$\mathrm{Co(III)} + \mathrm{DFO} \overset{k_{\mathrm{cat},1}}{\rightarrow} \mathrm{product\ 1} + \mathrm{Co(II)} \tag{6}$$

$$\mathrm{Fe(III)} + \mathrm{e} \rightleftarrows \mathrm{Fe(II)} \tag{7}$$

$$\mathrm{Fe(III)} + \mathrm{DFO/product\ 1} \overset{k_{\mathrm{cat},2}}{\rightarrow} \mathrm{product\ 2} + \mathrm{Fe(II)} \tag{8}$$

DFO is also electroreactive on carbon-based electrodes. It is oxidized on both u-CPE and nc-CPE and represents an anodic peak in the voltammograms, as depicted in Fig. 5a and b. However, it should be noted that its electrooxidation product(s) was (were) adsorbed on the electrode surface; this fact is evidenced by consecutive voltammograms of DFO recorded using u-CPE and nc-CPE in PBS (Fig. 5a and b). As can be seen, the anodic peak currents resulted from direct electrooxidation of DFO on u-CPE and nc-CPE lowered upon prolonged potential cycling. Therefore, the u-CPE and nc-CPE surfaces were fouled during the oxidation process so these electrodes are not suitable for development of an analytical procedure for DFO analysis. Consecutive cyclic voltammograms of DFO using n-CPE, however, represents no significant decreases in the currents (Fig. 5c) and so, n-Fe_2O_3@NaCo[$Fe(CN)_6$] oxidizes DFO without any surface fouling effect. This is important from the viewpoint of reproducibility of the data during analysis.

n-Fe_2O_3@NaCo[$Fe(CN)_6$] nanoparticles are stably distributed on the carbon surface, which can be readily and completely used as electrocatalytic units. These nanoparticles are often irregularly shaped objects, hence there are some defect sites, such as steps that separate planar atomic terraces, or kinks where a step advances or recedes, exposing corner or edge atoms on a plane. The enhancement of the reactivity of these defect sites can be so large that their presence determines—to a very large extent—the catalytic activity of a material.

Figure 6a illustrates cyclic voltammograms of 23.8 μM DFO in PBS using n-CPE recorded at different potential

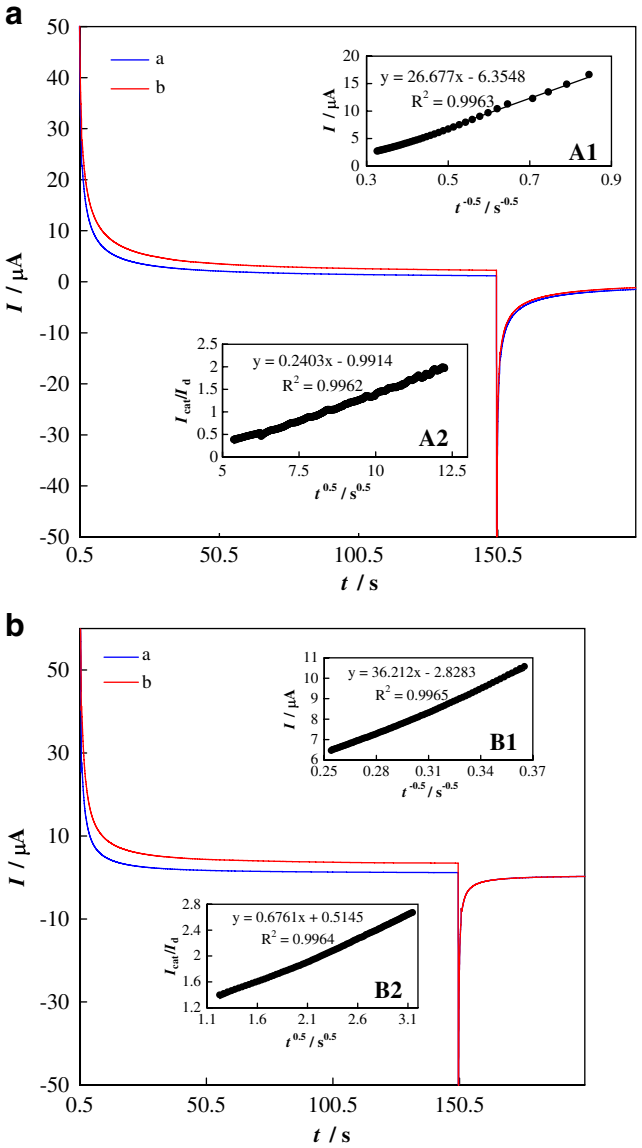

Fig. 7 **a** Double-step chronoamperograms for n-CPE in the absence (*a*) and presence (*b*) of 14.5 μM DFO recorded using potential steps of 600 and 300 mV, respectively. *Inset A1* Dependency of I on $t^{-1/2}$. *Inset A2* Dependency of I_{cat}/I_d on $t^{1/2}$. **b** Double-step chronoamperograms for n-CPE in the absence (*a*) and presence (*b*) of 14.5 μM DFO recorded using a potential step of 980 and 650 mV, respectively. *Inset B1* Dependency of I on $t^{-1/2}$. *Inset B2* Dependency of I_{cat}/I_d on $t^{1/2}$

sweep rates. The currents of both anodic peaks increased linearly with the square root of the potential sweep rate (Fig. 6, insets b and c), which indicates that the electrocatalytic processes were diffusion-controlled in the bulk of solution (vide infra). In addition, the value of electron transfer coefficients for the reactions can be obtained from the following equation [36]:

$$E_p = (RT/2\alpha F)\ln v + \text{constant} \quad (9)$$

which is valid for a totally irreversible diffusion-controlled process (vide infra). Using the dependencies of anodic peak potentials on the natural logarithm of the potential sweep rate (Fig. 6 insets d (for transition I) and inset e (for transition II)), the values of electron transfer coefficients were obtained for the electrocatalytic oxidation of DFO for transition I as 0.51 and for transition II as 0.32. Another point observed in Fig. 6a is that upon increasing potential sweep rate, both anodic peaks shift positively which suggests the existence of kinetic limitations in the reactions between n-Fe_2O_3@NaCo $[Fe(CN)_6]$ and DFO. From the slope of the linear dependency of anodic peak I current on the square root of potential sweep rate, and using the Randles–Sevcik equation for totally irreversible electron transfer processes, it can be calculated the diffusion coefficients of DFO as follows [37]:

$$I_p = \left(2.99 \times 10^5\right) n^{3/2}\alpha^{1/2} A\, C\, D^{1/2} v^{1/2} \quad (10)$$

where n, A, C and D are the number of exchanged electrons, real surface area of the working electrode, bulk concentration and diffusion coefficient of the electroreactive species, respectively. The diffusion coefficient of DFO was obtained as 1.61×10^{-6} cm^2 s^{-1}.

Like other voltammetric techniques, chronoamperometry can be used for the study of mass transfer kinetics and obtaining heterogeneous catalytic rate constant in EC′ mechanism. These approaches are performed by setting the working electrode potential to the desired value [37]. Figures 7a and b show double-step chronoamperograms for n-CPE in the absence (a) and presence (b) of 14.5 μM DFO recorded using the potential steps of 600 and 300 mV, respectively (a, corresponds to transition I in Fig. 4) and 980 and 650 mV, respectively (b, corresponds to transition II in Fig. 4). Plotting net currents with respect to the minus square roots of time presented linear dependencies (Fig. 7a and b, insets A1 and B1). These linear dependencies indicate that diffusion-controlled processes were dominated for both oxidation steps in the bulk of solution, which were also confirmed by cyclic voltammetry (Fig. 6, insets b and c). By using the slope of these lines, the diffusion coefficient of DFO can be obtained according to Cottrell's equation [37]:

$$I = nFAD^{1/2}C\pi^{-1/2}t^{-1/2} \quad (11)$$

where D is the diffusion coefficient and C is the bulk concentration. The mean value of the diffusion coefficient for DFO was found to be 1.20×10^{-6} cm^2 s^{-1}. This is in accord with the value obtained using cyclic voltammetry.

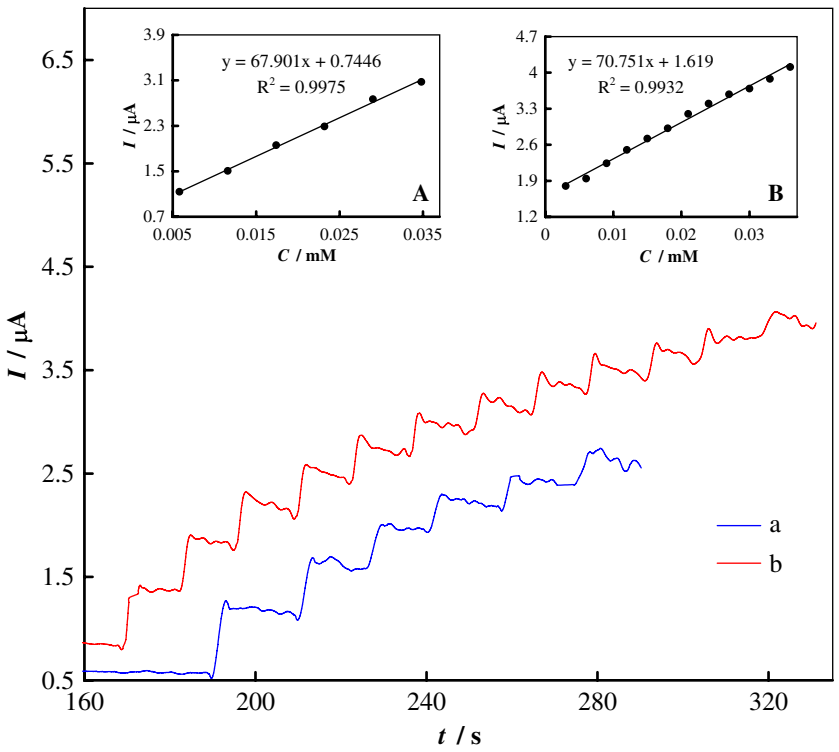

Fig. 8 Typical amperometric signals obtained during successive increments of DFO to PBS in batch system using the applied potentials of 480 (**a**) and 900 mV (**b**). Inset A: The corresponding calibration curve of amperometric signal represented as curve a in the main panel. Inset B: The corresponding calibration curve of amperometric signal represented as curve b in the main panel

Table 1 The determined parameters for calibration curves of DFO and accuracy and precision (n=3) for electrocatalytic oxidation on n-CPE in batch system

DC potential/mV	480	900
Linear range/μM	5.80–34.8	3.00–36.0
Slope/μA mM^{-1}	67.90	70.75
Intercept/μA	0.74	1.62
LOD/μM	0.32	0.28
LOQ/μM	1.00	0.92
RSD/%	0.40	0.18

Chronoamperometry can also be used to evaluate the catalytic rate constant according to [37]:

$$I_{cat}/I_d = \gamma^{1/2}\left[\pi^{1/2}\mathrm{erf}\left(\gamma^{1/2}\right) + \exp(-\gamma)/\gamma^{1/2}\right] \quad (12)$$

where I_{cat} and I_d are the currents in the presence and absence of DFO, $\gamma = k_{cat}Ct$ is the argument of the error function, k_{cat} is the catalytic rate constant and t is elapsed time. In the cases where $\gamma > 1.5$, the error function is almost equal to unity and the reaction zone is in the pure kinetic region, the above equation can be reduced to:

$$I_{cat}/I_d = \gamma^{1/2}\pi^{1/2} = \pi^{1/2}(k_{cat}Ct)^{1/2} \quad (13)$$

From the slopes of the I_{cat}/I_d versus $t^{1/2}$ plots, presented in Fig. 7a and b, insets A2 and B2, the mean values of catalytic rate constants were obtained as $k_{cat,1}=1.28\times10^6$ and $k_{cat,2}=8.05\times10^5$ cm^3 mol^{-1} s^{-1} for the first and second oxidation steps, respectively. So, Co(III) species is a catalyst almost ten times stronger than Fe(III) species, therefore it oxidizes DFO with a higher rate at lower potentials. It should also be added that as the electrolysis

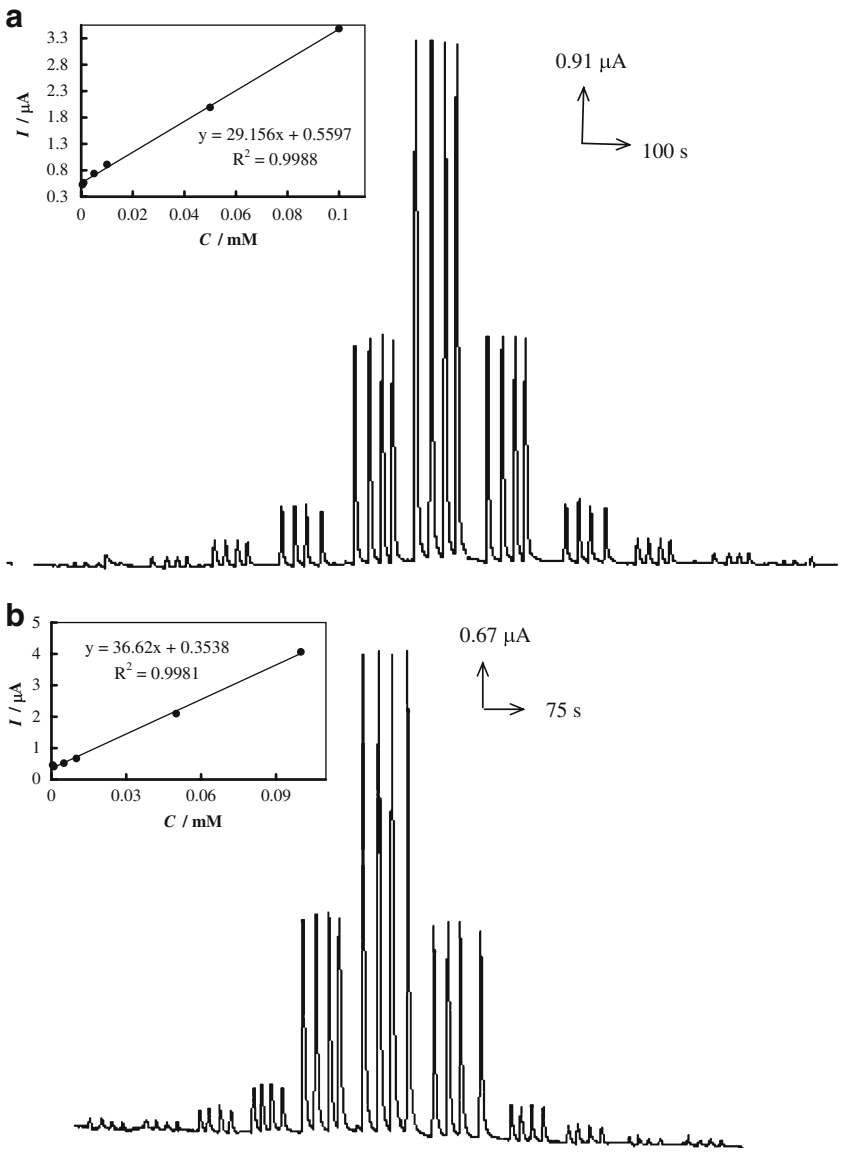

Fig. 9 **a**: Typical dynamic current responses to the injection of different DFO concentration at working potentials of 480 mV. Inset: The corresponding calibration curve. **b**: Typical dynamic current responses to the injection of different DFO concentration at working potentials of 900 mV. Inset: The corresponding calibration curve

potentials are stepped down to 300 or 650 mV, no significant currents are obtained indicating the irreversibility of the electrocatalytic oxidation processes occurred in transitions I and II.

Electrocatalytic reactions based on the surface mediation electron transfer processes (EC′ mechanisms) have been recently studied and formulated [4, 6, 38, 39]. A kinetic model based on this mechanism has been developed for the electrocatalytic oxidation of some biologically active compounds on some modified electrode surface and the faradaic current was calculated [4, 38, 39]. According to the model, the immobilized redox species on the electrode surface principally flip-flops between various valence states under the effect of external electric field. It is followed by the chemical reaction occurred at the surface of the modified electrodes/solution interface. Usually, the steady-state approximation for the reaction intermediates is dominated and the reaction is under the control of charge-transfer. Also, at high overpotentials, the diffusion of the substrate in the solution can be dominated [4, 38, 39]. Based on that model, there is no direct relationship between the catalytic current and the catalytic rate constant. On the other hand, both forward and backward rate constants of the redox transitions of the mediator are involved in the current [4, 38, 39]. The conditions described for this model also dominated this study. Meanwhile, the value of catalytic rate constant for the first step of the DFO oxidation is higher than that of the second step. However, this does not guarantee the higher catalytic current for the first step. This fact is evident from cyclic voltammograms represented in Fig. 4, curve b. Based on the model, the values of the catalytic rate constant and forward and backward rate constants for the redox transitions of the mediator can be changed in a manner that they generate similar catalytic current for a reaction with different catalytic rate constants.

In order to develop a simple procedure for the analysis of DFO, the technique of amperometry was used. Typical amperometric signals obtained during successive increments of DFO to PBS in batch system using the applied potentials of 480 (a) and 900 mV (b) are depicted in Fig. 8. Gentle stirring for a few seconds was needed to promote solution homogenization after each injection. The electrode response is quite rapid and proportional to the DFO concentration. In addition, amperometry at both potentials has near the same sensitivities (see also the catalytic currents in Fig. 4, curve b). The limits of detection (LOD) and quantitation (LOQ) of the procedure were calculated according to the 3SD/m and 10SD/m criteria, respectively, where SD is the standard deviation of the intercept and m is the slope of the calibration curves [40]. The determined parameters for calibration curves of drugs (Fig. 8, insets A and B), accuracy and precision, LODs and LOQs and the slopes of calibration curves in batch system are reported in Table 1.

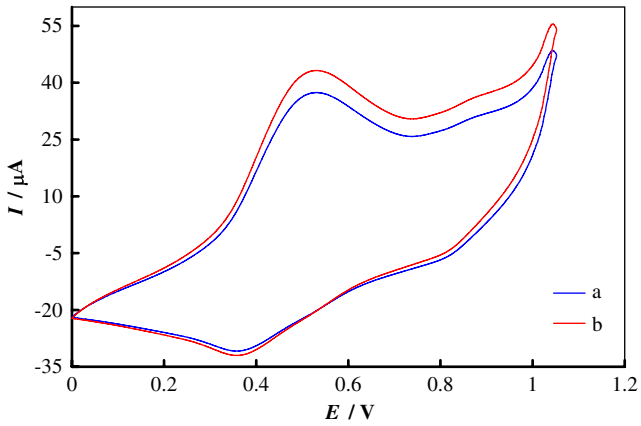

Fig. 10 Typical cyclic voltammograms recorded using n-CPE in the absence (**a**) and presence (**b**) of 88.5 μM $[Fe(DFO)_3]^{2+}$ in PBS

Flow injection analysis of DFO was also applied for assessing response and overall analytical performance of the method. Figure 9 exhibits typical dynamic current responses to the injection of different DFO concentration at working potentials of 480 (a) and 900 mV (b). The peak heights of the currents are proportional to the concentration of DFO (insets). The response of the electrode is linear over the entire 0.5–100 μM concentration range. The determined parameters for calibration curves of DFO are reported in Table 2.

The development of an electrochemical method for the determination of DFO in human serum blood was attemp-

Table 2 The determined parameters for calibration curves of DFO and accuracy and precision (n=3) for electrocatalytic oxidation of DFO on n-CPE in flow system

DC potential/mV	480	900
Linear range/μM	0.50–100	0.50–100
Slope/μA mM^{-1}	26.16	36.62
Intercept/μA	0.56	0.35
LOD/μM	0.12	0.08
LOQ/μM	0.42	0.26
RSD/%	1.54	2.71

Table 3 Results obtained for deferoxamine-iron complex analysis from spiked human serum samples

DC potential/mV	480	900
Linear range/μM	100–600	100–700
Slope/μA mM^{-1}	7.0	2.1
Intercept/μA	0.23	2.71
LOD/μM	0.28	0.28
LOQ/μM	0.94	0.92
RSD/%	2.32	3.03

ted. DFO, as an iron chelator, forms a 1:3 complex with iron ion ($[Fe(DFO)_3]^{2+}$) in the human body and the metabolic product of DFO is its complex [41]. Therefore, the complex should be analyzed in the biological fluids. Figure 10 shows cyclic voltammograms recorded using n-CPE in the absence (a) and presence (b) of 88.5 μM $[Fe(DFO)_3]^{2+}$ in PBS. Like the drug, its iron complex was also oxidized via both Co(III) and Fe(III) catalysts. Then, amperometric signals of DFO–iron complex spiked to serum sample were recorded. The probable poor selectivity of the method can pose problems in the analysis of biological samples, if they contain oxidizable substances. However, no current due to oxidation of the compounds in the employed serum samples was detected. The results obtained from our amperometric technique for determining DFO–iron complex in a serum sample are listed in Table 3.

In order to verify the durability and long-term stability of the n-CPE, 100 consecutive cyclic voltammograms using this electrode were recorded in PBS. It was found that the peak currents changed slightly (<5%). In addition, the electrode was stored in PBS when not in use and retained its electroreactivity for 4 weeks.

Conclusion

Nanoparticles of Fe_2O_3 core-$NaCo[Fe(CN)_6]$ shell were successfully synthesized. Then, the electrocatalytic oxidation of DFO was studied in the PBS, pH 7.4, using carbon paste electrodes modified by these core-shell nanoparticles. Using cyclic voltammetry and chronoamperometry techniques, the kinetic parameters of DFO such as charge-transfer coefficient, catalytic reaction rate constant, and diffusion coefficient for oxidation were determined. The electrocatalytic processes are diffusion-controlled in the bulk of solution. An amperometric procedure was successfully applied to the quantification of DFO in bulk form and human biological fluids. The simplicity, sensitivity, selectivity, and short time of analysis are the main advantages of this procedure.

Acknowledgments The financial support of the Research Councils of Islamic Azad University and K. N. Toosi University of Technology are gratefully acknowledged.

References

1. Kontoghiorghes GJ (1995) Toxicol Lett 80:1
2. Heli H, Jabbari A, Zarghan M, Moosavi-Movahedi AA (2009) Sens Actuate B 140:245
3. Heli H, Hajjizadeh M, Jabbari A, Moosavi-Movahedi AA (2009) Anal Biochem 388:81
4. Heli H, Hajjizadeh M, Jabbari A, Moosavi-Movahedi AA (2009) Biosens Bioelectron 24:2328
5. Heli H, Jabbari A, Moosavi-Movahedi AA, Tabeshnia M (2009) Chem Anal 45:619
6. Heli H, Jabbari A, Majdi S, Mahjoub M, Moosavi-Movahedi AA, Sheibani S (2008) J Solid State Electrochem 13:1951
7. Heli H, Zarghan M, Jabbari A, Parsaei A, Moosavi-Movahedi AA (2010) J Solid State Electrochem. In Press, doi:10.1007/s10008-009-0846-x
8. Heli H, Faramarzi F, Jabbari A, Parsaei A, Moosavi-Movahedi AA (2010) J Braz Chem Soc 21:16
9. Zhong CJ, Maye MM (2001) Adv Mater 13:1507
10. Heli H, Majdi S, Sattarahmady N (2009) Sens Actuators B, In Press, doi:10.1016/j.snb.2009.11.065
11. Heli H, Majdi S, Jabbari A, Sattarahmady N, Moosavi-Movahedi AA (2010) J Solid State Electrochem, In Press, doi:10.1007/s10008-009-0979-y
12. Wang J (ed) (1996) Electroanalytical techniques in clinical chemistry and laboratory medicine. VCH, New York
13. Jeerage KM, Steen WA, Schwartz DT (2002) Chem Mater 14:530
14. Kulesza PJ, Malik MA, Miecznikowski K, Wolkiewicz A, Zamponi S, Berrettoni M, Marassi R (1996) J Electrochem Soc 143:L10
15. Jayalakshmi M, Scholz F (2000) J Power Sources 91:217
16. Chen S-M (2002) J Electroanal Chem 521:29
17. Pournaghi-Azar MH, Sabzi R (2002) J Solid State Electrochem 6:553
18. Cai C-X, Ju H-X, Chen H-Y (1995) J Electroanal Chem 397:185
19. Xun ZY, Cai CX, Xing W, Lu T (2003) J Electroanal Chem 545:19
20. Golabi SM, Noor-Mohammadi F (1998) J Solid State Electrochem 2:30
21. Qian L, Yang X (2006) Talanta 69:957
22. Giorgetti M, Berrettoni M, Zamponi S, Kulesza PJ, Cox JA (2005) Electrochim Acta 51:511
23. Nakamoto K (1986) Infrared and Raman spectra of inorganic and coordination compounds. John Wiley & Sons, New York
24. Goubard F, Tabuteau A (2003) Struct Chem 14:257
25. Cullity BD (1978) Elements of X-ray diffraction. Addison-Wesley, Reading, MA
26. Liu H, Wang G, Park J, Wang J, Liu H, Zhang C (2009) Electrochim Acta 54:1733
27. Li-Hong S, Tian W, Mei-Jia W, Di L, Yuan-Jian Z, Jing-Hong L (2005) Chin J Chem 23:149
28. Wang B, Cao X (1991) J Electroanal Chem 309:147
29. Wang J, Golden T, Li R (1988) Anal Chem 60:1642
30. Richard Prabakar SJ, Narayanan SS (2006) Anal Bioanal Chem 386:2107
31. Lezna RO, Romagnoli R, De Tacconi NR, Rajeshwar K (2002) J Phys Chem B 106:3612
32. De Tacconi NR, Rajeshwar K, Lezna RO (2006) J Electroanal Chem 587:42
33. Itaya K, Ataka T, Toshima S (1982) J Am Chem Soc 104:4767
34. Krylov AV, Lisdat F (2007) Electroanalysis 19:23
35. Tao W, Pan D, Liu Y, Nie L, Yao S (2004) J Electroanal Chem 572:109
36. Harrison JA, Khan ZA (1970) J Electroanal Chem 28:131
37. Bard AJ, Faulkner LR (2001) Electrochemical methods. John Wiley and Sons, New York
38. Hajjizadeh M, Jabbari A, Heli H, Moosavi-Movahedi AA, Shafiee A, Karimian K (2008) Anal Biochem 373:337
39. Hajjizadeh M, Jabbari A, Heli H, Moosavi-Movahedi AA, Haghgoo S (2007) Electrochim Acta 53:1766
40. Miller JC, Miller JN (1994) Statistics for analytical chemistry. Ellis-Harwood, New York
41. Hider RC, Zhou T (2005) Ann N Y Acad Sci 1054:141